Key Points:

- Cusp scintillation occurrence increases significantly with rising geomagnetic activity
- The energy flux of soft electron precipitation in the cusp has a statistical tendency to decrease as geomagnetic activity increases
- The increase in cusp scintillation with geomagnetic activity must be caused by drivers other that soft electron precipitation

Correspondence to:
M. F. Ivarsen,
m.f.ivarsen@fys.uio.no

GNSS Scintillations in the Cusp, and the Role of Precipitating Particle Energy Fluxes

Magnus F. Ivarsen[1,2] [ID], **Yaqi Jin**[1] [ID], **Andres Spicher**[3] [ID], **Jean-Pierre St-Maurice**[2,4] [ID], **Jaeheung Park**[5,6] [ID], and **Daniel Billett**[2]

[1]Department of Physics, University of Oslo, Oslo, Norway, [2]Department of Physics and Engineering Physics, University of Saskatchewan, Saskatoon, SK, Canada, [3]Department of Physics and Technology, UiT The Arctic University of Norway, Tromsø, Norway, [4]Department of Physics and Astronomy, University of Western Ontario, London, ON, Canada, [5]Korea Astronomy and Space Science Institute, Daejeon, South Korea, [6]Department of Astronomy and Space Science, Korea University of Science and Technology, Daejeon, South Korea

Abstract Using a large data set of ground-based GNSS scintillation observations coupled with in situ particle detector data, we perform a statistical analysis of both the input energy flux from precipitating particles, and the observed occurrence of density irregularities in the northern hemisphere cusp. By examining trends in the two data sets relating to geomagnetic activity, we conclude that observations of irregularities in the cusp grows increasingly likely during storm-time, whereas the precipitating particle energy flux does not. We thus find a weak or nonexistent statistical link between geomagnetic activity and precipitating particle energy flux in the cusp. This is a result of a previously documented tendency for the cusp energy flux to maximize during northward IMF, when density irregularities tend not to be widespread, as we demonstrate. At any rate, even though ionization and subsequent density gradients directly caused by soft electron precipitation in the cusp are not to be ignored for the trigger of irregularities, our results point to the need to scrutinize additional physical processes for the creation of irregularities causing scintillations in and around the cusp. While numerous phenomena known to cause density irregularities have been identified and described, there is a need for a *systematic* evaluation of the conditions under which the various destabilizing mechanisms become important and how they sculpt the observed ionospheric "irregularity landscape." As such, we call for a quantitative assessment of the role of particle precipitation in the cusp, given that other factors contribute to the production of irregularities in a major way.

Plain Language Summary The cusp ionosphere is a particularly turbulent part of the interaction between Earth and the solar wind. Here, magnetic field lines connect the ionosphere directly to the solar wind, and a range of plasma physical mechanisms can studied. "Soft" (low-energy) electrons raining into Earth's atmosphere inside the cusp has been suggested several times in the past as an important contributor to the various energetic phenomena found in the cusp, but little evidence exists that can tell us how important they are. We present a large statistical study of the cusp's input energy (the soft electrons) and how it affects the cusp's turbulent output (widespread plasma irregularities). We find a discrepancy in that soft electrons largely exhibit opposite long-term trends compared to the cusp plasma turbulence. Put simplistically, the energy budget provided by soft electrons might not be sufficient to explain the enormous energy that are at times pent up in the ionospheric cusp plasma turbulence. These results point to the fact that the community needs to address the role of particle precipitation (electrons, but also ions) in producing the observed ionosphere "irregularity landscape."

1. Introduction

The cusp is a vital connection point for the solar wind-magnetosphere-ionosphere interaction (Saunders, 1989). There, a conspicuous ion outflow occurs through the magnetospheric cleft (Bell, 1981; Frederick-Frost et al., 2007; Li et al., 2012; Ogawa et al., 2003), intense soft electrons precipitate into the ionosphere (Liou et al., 2001; Newell et al., 2010; Shepherd, 1979; Titheridge, 1976), and intense small-scale field-aligned currents (FAC) occur (Rother et al., 2007). The cusp ionosphere also has an abundance of plasma density irregularities over a wide range of spatial scales (Dyson et al., 1974; Tsunoda, 1988). Due to the tendency for irregularities to cause radio scintillations, those irregularities can severely disrupt the performance of the Global Navigation Satellite System (GNSS, Kintner et al., 2007). Recently, the studies of ionospheric irregularities and GNSS scintillations have garnered more interest (e.g., Jin et al., 2015; Mitchell et al., 2005; Oksavik et al., 2015; Prikryl

et al., 2015; Spogli et al., 2010). Throughout this manuscript, we will only use phase scintillations as they are more common at high latitudes, and we shall use GNSS scintillations as a proxy for ionospheric irregularities (e.g., Meziane et al., 2023).

Scintillations are recorded when the GNSS radio signal passes through turbulent plasma structures in the ionosphere (Yeh & Liu, 1982). Since the GNSS scintillation receivers are fixed on the ground, scintillation observations will be sensitive to low-amplitude fast-growing irregularities and high-amplitude slow-growing irregularities alike, regardless of how long-lived those irregularities are, as long as the small-scale fluctuations (on the order of ~ a few kilometers) induced in the plasma are sufficiently intense. Absolute density fluctuations (as opposed to relative fluctuations) are most important (Aarons et al., 1981; Jin et al., 2018). The scintillation-inducing fluctuations in plasma density are thought to be caused by turbulent redistribution of irregularity power (Hamza et al., 2023). As such, scintillations are in general triggered by ionospheric irregularities over a *wide range of spatial scales* (Jin et al., 2014; Kintner et al., 2007; van der Meeren et al., 2014), though specific irregularity scale sizes become an important factor in determining whether amplitude and/or phase scintillations are triggered (e.g., Song et al., 2023).

There are two distinct main scenarios that have been considered regarding the formation of ionospheric irregularities in the cusp ionosphere (Jin et al., 2017). One is during relatively quiet times, when no classical polar cap patches (or Tongue Of Ionization, TOI) are created in the cusp region. The other is invoked for more disturbed conditions, when the expanded ionospheric convection brings in high density plasma from the sunlit sub-auroral region to form polar cap patches (Carlson, 2012; Lockwood & Carlson Jr, 1992). For the first scenario, Kelley et al. (1982) proposed that the soft electron precipitation is an important source of large-scale (>10 km) ionospheric structures in the cusp region. Sharp density gradients on the edges of such large structures then feature in plasma instability processes, such as the Gradient Drift Instability (GDI, Tsunoda, 1988), to create smaller scale ionospheric irregularities (Moen et al., 2002). This basic process is thought to explain why soft electron precipitation should be important for the production of irregularities in the cusp. Case studies using in situ measurements by sounding rockets and satellites in low-Earth-orbit later confirmed that soft electron precipitation is indeed a source of ionospheric irregularities in the cusp ionosphere (Goodwin et al., 2015; Jin et al., 2019; Moen et al., 2012; Spicher et al., 2015). These case studies were conducted during relatively quiet times, typically during deep winter when the solar terminator is significantly equatorward of the high-latitude convection throat, where classical high-density polar cap patches do not form. We note that although some events meet the criteria that electron density inside a plasma patch be at least two times higher than the background density (Crowley, 1996), the absolute density in these cases can be relatively low ($1–2 \times 10^{11}$ m^{-3}). Such low-density patches are termed "baby" patches by Hosokawa et al. (2016), since they are created by auroral structures such as Poleward Moving Auroral Forms (PMAF, Sandholt et al., 1986, 1998).

In a more recent study, Jin et al. (2017) directly compared the ionospheric irregularities for the two scenarios with and without classical polar cap patches in the cusp region. The authors demonstrated that while soft electron precipitation can create weak to moderate GNSS scintillations, occurrence rates for the latter are *significantly* enhanced in the cusp ionosphere when classical polar cap patches are present. The differing results depending on whether there are patches present in the cusp were explained by the combined effect of polar cap patches and cusp dynamics: while polar cap patches provide the main body of high-density plasma, cusp dynamics act to structure the patches on smaller scales. In this respect, flow shears (Basu et al., 1990; Spicher et al., 2020), intense small-scale FACs (Lühr et al., 2004), and auroral precipitation (Moen et al., 2012; Oksavik et al., 2015) have all been shown to play significant roles in generating ionospheric irregularities. In other words, the menagerie of processes and mechanisms capable of producing cusp irregularities contain many specimens, of which soft electron precipitation is often highlighted as an important source of both ionization and free energy. However, there is a need to assess the relative importance and separate contribution of each source of free energy and under which geomagnetic conditions a particular mechanism prevails or even dominates.

On top of the need to identify the relative importance of shears, FACs and precipitation for the triggering of plasma instabilities, there is a need to address another question that is likely related to the interplay between these destabilizing factors, namely, the stark contrast reported in the literature between the seasonal variations in the cusp between soft electron precipitation and the occurrence of scintillation. For one thing, the dayside number flux of precipitating electrons and ions largely maximizes during local summer (Newell & Meng, 1988b; Newell et al., 2010), and during geomagnetically quiet conditions (Newell et al., 2009). This seasonal effect is some-

times explained by the impact of dayside Pedersen conductance, which strongly depends on the incident sunlight (Brekke & Moen, 1993; Vickrey et al., 1981), whereas the preference for geomagnetic quiet conditions can be explained by a preference for northward IMF on the dayside (Newell et al., 2009). On the other hand, in opposition to the inferred cusp precipitation trend, climatological studies of GNSS scintillations show that scintillation occurrences in the cusp are higher during local winter and during geomagnetically active conditions (Alfonsi et al., 2011; Jin et al., 2015; Prikryl et al., 2015).

In order to add more substance to the cusp irregularity generation question and to shed light on what appears to be opposite seasonal trends, we have put together a statistical analysis of two large data sets of both in situ observations of particle precipitation by Defense Meteorological Satellite Program (DMSP) satellites and ground-based GNSS scintillation data in the northern hemisphere. From the DMSP satellites' particle detector instrument we collected data from 52,000 crossings over the high-latitude northern hemisphere made during 3 years near the peak of the 24th solar cycle (2014–2016). For the same time period, we also collected continuously recorded GNSS scintillation indices from three GNSS stations located in Svalbard, Norway. Through a statistical aggregation, and through direct in situ detection of the cusp, we demonstrate that the energy flux of precipitating particles decreases in the cusp during local winter and actually tends to *decrease* as geomagnetic activity increases, though with a very large spread around that decrease. At the same time, we demonstrate that the scintillation occurrence rate increases drastically with increasing geomagnetic activity. The lack of statistical association between irregularities and particle precipitation in the cusp reinforces earlier suggestions that processes/sources other than soft electron precipitation are playing a key role in creating the more intense scintillation that is observed in the cusp during geomagnetically active times.

2. Instrumentation and Methodology

There are two aspects to the methodology used in this study. First is a database of precipitating electron and ion data from the SSJ instrument on the F16, F17, F18, and F19 satellites of the DMSP. The DMSP satellites are in helio-synchronous dawn-dusk polar orbits at an altitude of around 840 km, covering most of the region of interest to the present paper, the dayside high-latitude ionosphere in the northern hemisphere. The SSJ instrument uses particle detectors to measure the energy flux of precipitating electrons and ions through 19 energy channels from 30 eV to 30 keV, with a cadence of 1 s (Redmon et al., 2017). We characterize soft electron precipitation by integrating over energy channels from 30 to 650 eV, following the method outlined in Redmon et al. (2017). We classify each precipitating particle spectrum whenever we find it to be directly sampled in the cusp, following a widely used definition of the cusp given by Newell and Meng (1988a). This means that a cusp datapoint is defined as having an average electron energy lower than 220 eV, and an average ion energy higher than 300 eV and lower than 3,000 eV. In addition, the electron energy flux through channels 2 and 5 keV should be lower than 10^7 keV cm^{-2} s^{-1}ster^{-1}, and the total integrated ion energy flux should exceed 2×10^9 keV cm^{-2} s^{-1}ster^{-1}. The different satellites exhibit slightly different energy fluxes statistically, which is likely due to instrument calibration. However, after testing, we have concluded that the slight measurement variations do not influence the results in any systematic way. Note that "total integrated energy flux" refers to differential energy flux integrated across energy channels and is denoted JETOT in the figures.

Figure 1 shows an example of a pass through the cusp by DMSP F19, where all the mentioned criteria are met. The data were obtained around 06:45 UT on 6 December 2014. Panel (a) shows the orbit, and panels (b) and (c) show electron and ion energy flux respectively, with the cusp precipitation "patch" indicated by a black square. In this case, the cusp datapoint stretches over an orbital stretch of 85 s, corresponding to 646 km of distance. This is double the median size of a typical cusp crossing in the data set, which is around 40 s of data per pass (excluding passes where the cusp was not detected at all). Data such as that shown in Figure 1 are used in the analysis to come, but first we need to introduce the scintillations data set used in the present study.

The scintillation database comes from ground-based observations of the σ_ϕ radio index, using vertical phase scintillation calculations (Jin et al., 2018; Spogli et al., 2013). We perform these calculations on data from three GNSS receivers on Svalbard, Norway (Oksavik, 2020), located in Ny Ålesund (78.9°N, 11.9°E), Kjell Henriksen Observatory (78.1°N, 16°E), and Bjørnøya (74.5°N, 19°E). We selected a 30° elevation cut-off and an ionospheric piercing point altitude of 350 km, and used satellites from the GPS and Galileo systems. The total time period for the two data sets in the present study stretches from 2014 through 2016, and roughly captures the 24th solar cycle peak. We consider northern hemisphere observations collected in all seasons, where we define
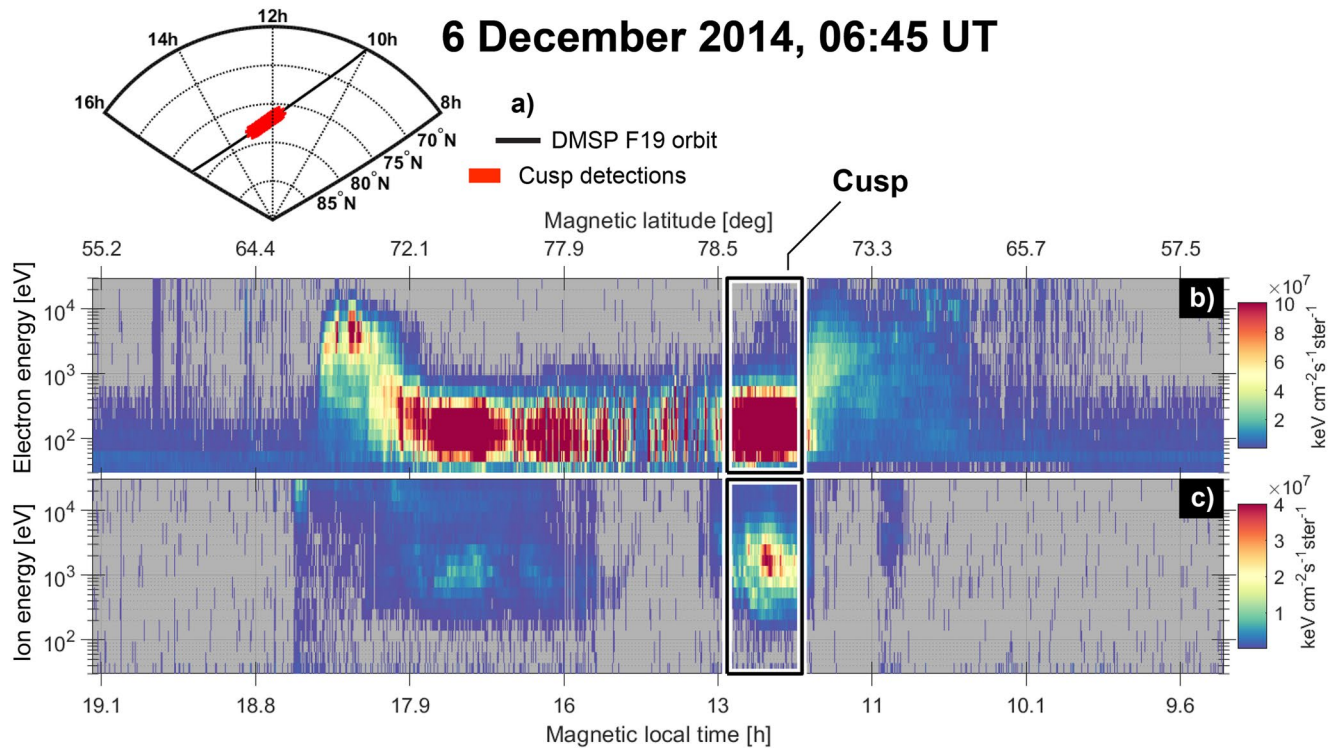
Figure 1. Panel (a): a DMSP F19 pass through the cusp on 6 December 2014. Red markings show cusp detections. Panels (b) and (c): electron and ion energy flux with particle energy along the *y*-axes, and two *x*-axes showing MLAT (top) and MLT (bottom).

a season as a 90-days period centered on a solstice in the case of summer or winter, with the rest classified as equinox.

We collected and stored the quantities covered above, and also extracted the value of several geomagnetic indices and solar wind-magnetosphere-ionosphere coupling functions, with the goal of quantifying the ebb and flow of solar wind-energy being injected into the ionosphere. To start with, we used the SME-index, which provides a global assessment of the intensity of Hall currents from several hundred ground-based stations in the auroral electrojet, and is therefore able to provide a global view of the geomagnetic activity resulting from the coupling with the solar wind which starts at the cusp (Cowley, 2000). The SME-index has indeed been shown to accurately quantify the total auroral energy input into the nightside aurora (Gjerloev, 2012; Newell & Gjerloev, 2011). We also considered the Sym-H index, which measures the storm-time ring current (Wanliss & Showalter, 2006) and is widely used to characterize magnetic storms. However, the SME-index is useful not just for storms but also for magnetospheric substorms that need not be part of clearly identifiable storm. From space, we collected observations of the interplanetary magnetic field (IMF) and solar wind, using 1-min OMNI data timeshifted to the bowshock (Papitashvili & King, 2020). Based on the latter, we calculated the so-called Newell coupling function, namely, the rate at which magnetic flux is opened at the magnetopause ($d\Phi/dt$, Newell et al., 2007). We also computed the so-called Kan-Lee electric field, which quantifies "the power delivered by the solar wind dynamo to the open magnetosphere" (Kan & Lee, 1979, p. 577).

3. Results

First, we aggregated DMSP data along with scintillation indices from Svalbard. This resulted in Figure 2, which displays the entire data set in terms of 18 climatological maps of the high-latitude dayside ionosphere. Here, all data are plotted using magnetic local time (MLT) and magnetic latitude (MLAT) as coordinates (Baker & Wing, 1989). In each spatial bin, we took the occurrence rate of $\sigma_\phi > 0.15$ rad events, and the median soft electron energy flux obtained from an integration over channels lower than 1 keV. Panels (a–i) show the GNSS scintillation occurrence rate and panels (j–r) the median integrated soft electron flux. Each row represents a local
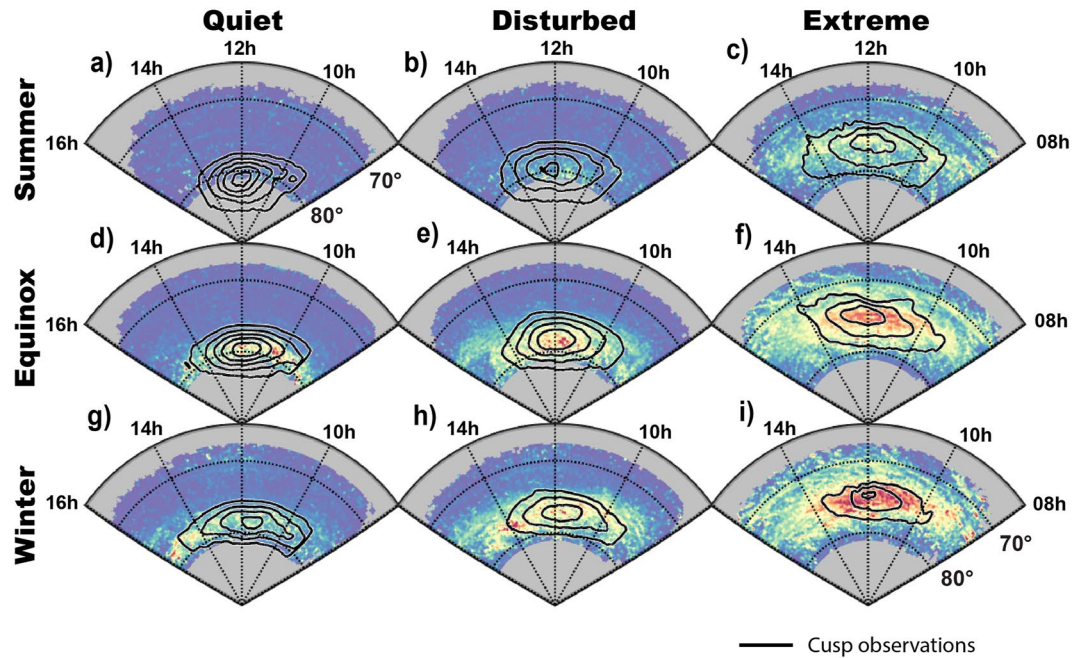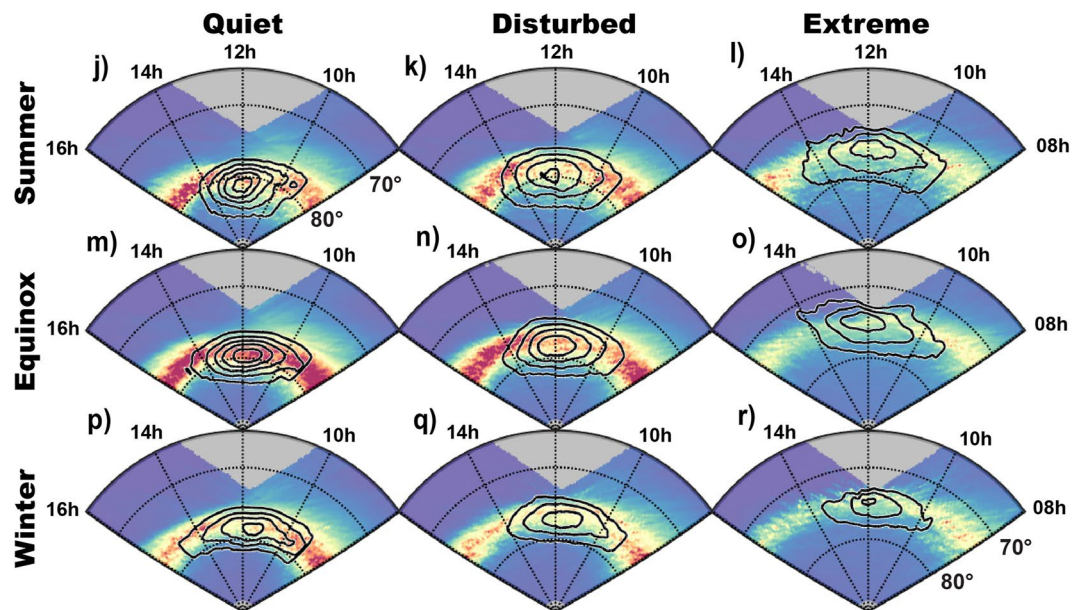
Figure 2. A northern hemisphere climatology of GNSS scintillation occurrence (panels a–i) and median integrated soft electron flux (panels j–r). Each row represents a local season (e.g., a–c show summer while g–i show winter), and each column represents geomagnetic activity in three SME-index bins with equal population counts. Black lines show where cusp datapoints were encountered, with occurrence rates from 10%, 20%, and so forth, until 50%, with the 10%-line always being the outermost contour.

season and each column shows geomagnetic disturbance binned by the SME-index. Each map shows data binned in MLT and MLAT (>65°), with noon pointing upwards and dawn-side to the right. GNSS scintillation occurrence rates are calculated by taking the proportion of σ_ϕ index values greater than 0.15 in each bin. A color scale is used to identify intensity levels, with gray to signify a lack of data.

The three columns in Figure 2 indicate the following different geomagnetic disturbance levels; an SME-index value lower than 103 nT, indicative of quiet observations; between 103 and 234 nT indicative of disturbed conditions; and a value greater than 234 nT to characterize *extreme* situations. These are the 33rd and 67th percentile value of the SME-index for the years 2014–2016, and so the three categories constitute a third of the total data set each, and the extreme category features a median SME-index value of 400 nT. Note that further discussion concerning the usefulness of the SME-index is provided in an appendix to this paper. Suffice to say that an analysis that bins the data using any of the indices mentioned so far does produce similar results (we refer also to Figure 4 later). Lastly, note that in all panels, a series of black contour lines indicates the distribution of DMSP datapoints having a cusp-occurrence rate greater than 10%, 20%, and so forth, until 50%. The 10%-line is always the outermost contour. As most bins have in fact less than 50% cusp datapoints, the median conditions are unlikely to reflect the cusp. The precipitating particle data presented in Figure 2 thus shows a *dayside* or *noon-sector* climatology.

Quiet time observations of the dayside (first column) are characterized by an overall low occurrence of GNSS scintillations and a high flux of soft electrons, especially for the equinoxes. During disturbed conditions (second column), strong GNSS scintillations occur more frequently at MLATs exceeding 75°, while the flux of soft electrons seems to *diminish* slightly compared to quiet times. Finally, during extremely active conditions (third column), GNSS scintillation occurrence reaches a clear peak in each season, at which point the dayside soft electrons seem to have reached a clear minimum. Indeed, panel (i) of Figure 2 contains fully one third of all $\sigma_\phi > 0.15$ rad events in our database, despite containing a clear minimum in the dayside soft electron energy flux.

However, as mentioned, occurrence rates for direct observations of the cusp are relatively low, and so to investigate conditions inside the cusp we will now show the results from performing a statistical analysis on all 1 million datapoints that were determined to be inside the cusp proper, using the Newell and Meng (1988a) definition described above. We start by binning the data set by the IMF B_Z (Figure 3), followed by binning the data set in all five geomagnetic indices in turn (Figure 4). In the figures to come, we only show *winter* cusp-detections, as scintillations maximize during this season. Later, in the discussion section (Figure 5), we shall show an analysis of the seasonal trends behind cusp-electron energy flux and scintillation occurrence.

Returning to the task at hand, in Figure 3 we present an analysis where we now bin winter cusp detections by IMF B_Z (taking the 30-min median value to account for distance traveled from the bowshock). In the first column, we plot the prevalence of density irregularities, represented by the occurrence rate of $\sigma_\phi > 0.15$ rad events occurring within 2° MLAT of the average latitudinal cusp locations. Each panel in the first column corresponds to one of seven B_Z bins, where the first and the last bins contain 15% of the data set on both ends of the distribution, with the remaining bins linearly spaced between those two extreme bins. This way, each bin contains roughly the same number of observations. We integrate over MLAT and plotting the data as functions of MLT (*x*-axis). The next two columns show the precipitating electron (second column) and ion (third column) energy flux, with energy channel along the *y*-axes. We plot the median energy flux through each energy channel for each local time. The "severe northward IMF"-bin ($B_Z > 2.7$ nT) is on the top of the page, while the extreme opposite bin ($B_Z < -2.7$ nT) is located on the bottom, with the center bin corresponding to $|B_Z| < 0.6$ nT.

From the fourth bin (Figure 3j) and downwards, there is a clear and systematic increase in GNSS scintillations. At the same time, for both ions and electrons, the magnitude of the precipitating particle energy flux is decreasing monotonically from the top-most bin to the bottom. The same is true for the number flux (which we show in Figure S1). This clearly indicates that scintillation occurrence and particle precipitation follow opposite trends in terms of the IMF B_Z: the more southward the IMF is, the greater the scintillation occurrence whereas the same IMF changes mark a steady decrease in energy fluxes of both electrons and ions.

For a more in-depth exploration of this result, we applied the foregoing analysis to five geomagnetic indices or coupling functions. Figure 4 summarizes the results using the SME-index, the Sym-H-index, the Newell coupling function, the Kan-Lee electric field, and the IMF B_Z. Similarly to Figure 3, we used seven bins for each index, with the first and last bins containing 15% of the data set on both ends of the distribution, while the remaining
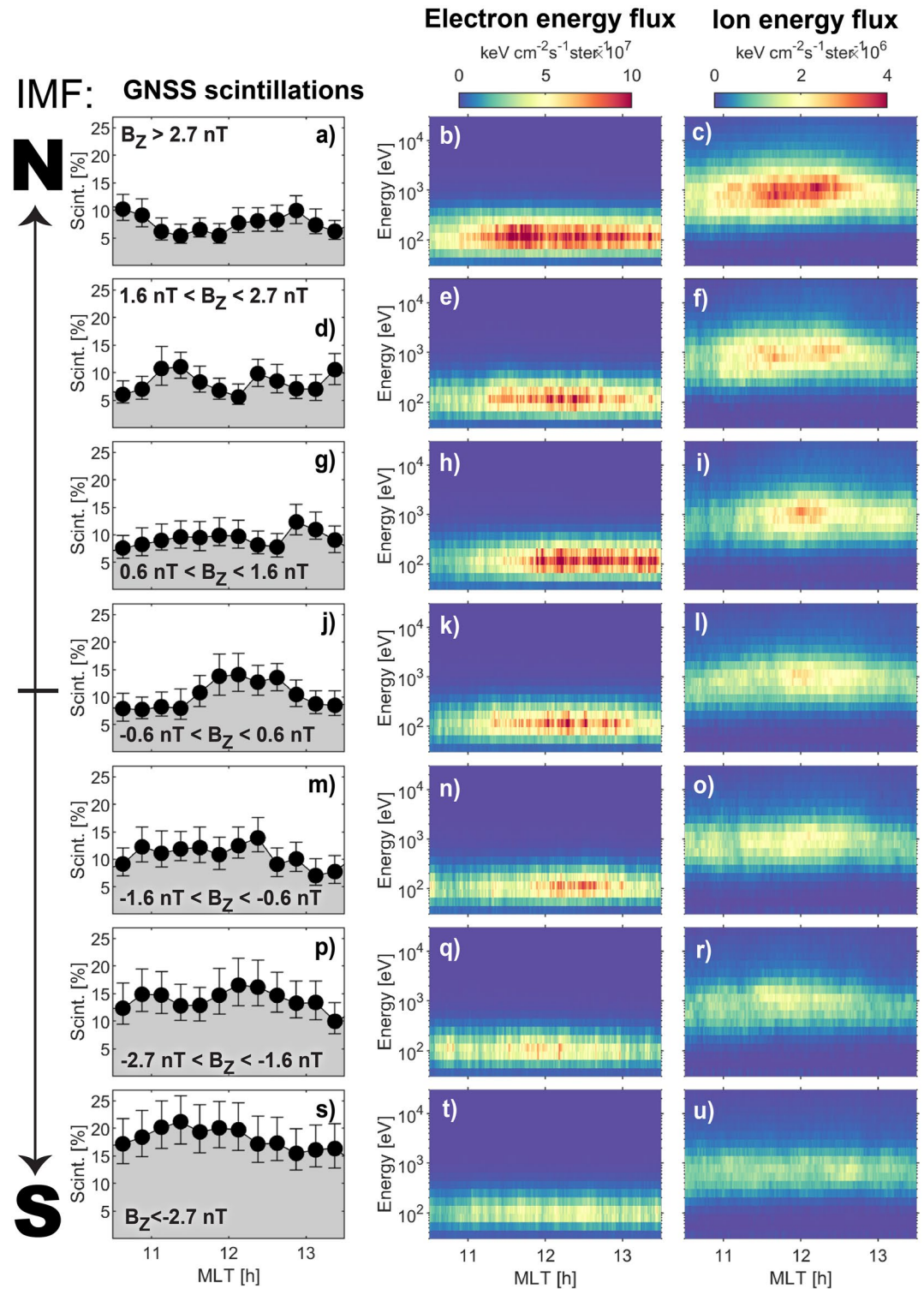
Figure 3. Local time slices through six IMF bins for the cusp. Each IMF B_Z bin aggregates a roughly equal number of orbital winter passes through the northern hemisphere cusp. The first column shows median GNSS scintillations, the second, the median contents of the various electron energy flux channels, and the third shows the same thing, but for the ion energy flux.

bins were chosen to be linearly spaced between those two extremes. We considered a data subset that contained winter DMSP cusp data and did not include other data devoid of satellite cusp crossings. Panels (a)–(e) show the resulting probability distributions that we obtained for the data subset. Panels (f)–(j) show, for each of the
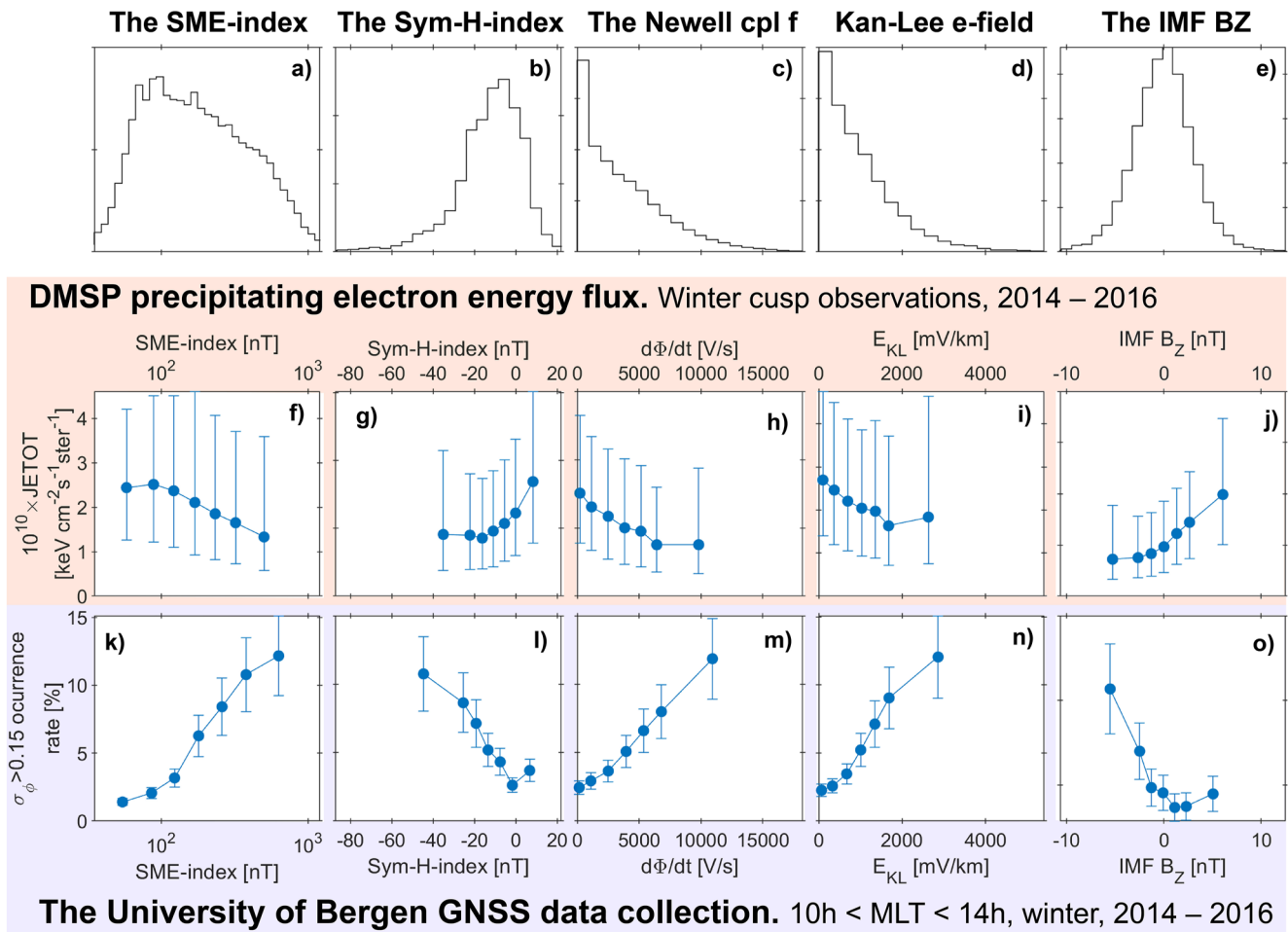
Figure 4. Panels (a) through (e): probability distributions of five different indices or coupling functions as measured during the time period selected for this study. Panels (f) through (j): median DMSP electron energy flux recorded as a function of the changes in the various indices, errorbars denote upper/lower quartile distributions. Panels (k) through (o): change with the various index values of the proportion of events for which the phase scintillation index σ_ϕ exceeded 0.15 rad, with errorbars based on the underlying σ_ϕ deviation.

seven bins, the distribution found in the total integrated electron energy flux using only spectra that were inferred to strictly originate from the cusp. Panels (k)–(o) likewise present the binned occurrence rate of $\sigma_\phi > 0.15$ rad obtained between 10.5 and 13.5 hr MLT. Note that each panel has what amounts to the same limits along the x-axis: we show all data between the 0.5th percentile value of each index to the left and the 99.5th percentile value on the right.

Figure 4 shows that, owing to the smaller scatter (vertical errorbars) about the median values, the best of the five indices/coupling functions to parameterize precipitation in the cusp is actually the IMF B_Z. We also notice that when the SYM-H indicates a magnetic storm (values less than −20 nT) the energy flux in the cusp is at its minimum. However, this should correspond to larger SME values, which does a better job at relating to the cusp electron energy flux. This being stated, the SME does a better job than the IMF B_Z at predicting scintillations while it remains an adequate predictor of energy deposition by particles in the cusp when it exceeds 100 nT. Interestingly, the indices most directly related to the cusp, namely, $d\Phi/dt$ and E_{KL}, are extremely good statistical predictors of the scintillation activity, but the quiet-most bins in panels (m) and (n) are higher than the quiet-most bin in panel (k), meaning that the SME-index is best at separating the scintillations database. Like the other indices (except for B_Z), they predict that on average the cusp precipitation energy goes down as they take more extreme values, but, like the SME case, the scatter about the median remains considerable when it comes to precipitating energy flux.

One important fact remains clear from Figures 3 and 4: no matter what is used to characterize magnetic activity in relation to cusp dynamics, whenever the intensity of scintillations in the cusp goes up the energy flux at the

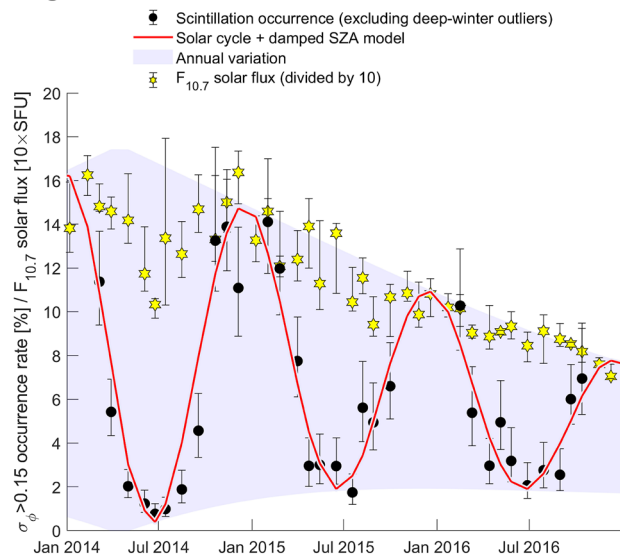## Long-term trends in scintillation event likelihood

Figure 5. The occurrence rate of scintillation events in the cusp-region, binned by Carrington rotations (27-day periods of solar rotation), for 10.5 hr < MLT <13.5 hr MLT over Svalbard. A composite model (solar cycle variation plus a damped solar zenith angle, Equation B3) is shown in solid red line, with annual variation during the solar cycle declining phase in shaded light blue area. Deep-winter outliers (see Appendix B) are removed from the long-term scintillation occurrence data. In yellow hexagrams are shown the median $F_{10.7}$ solar flux for each Carrington rotation, in solar flux units divided by 10.

cusp does not increase and in fact goes down on average, except for the slight tendency for scintillations to increase during severely positive B_Z (Figure 4, panel o). In addition, the best controlling factor for energetic cusp particles is the IMF B_Z: when the IMF is increasingly northward, the energy deposited by particles in the cusp keeps increasing.

4. Discussion

In this study, we have parameterized GNSS scintillations and cusp precipitation energy fluxes by several measures of geomagnetic activity. The $\sigma_\phi > 0.15$ rad occurrence changes dramatically (from a rate of ∼1% to rate of ∼15%) following an increase in geomagnetic activity (Figure 4k through n). Conversely, the median energy flux of precipitating particles does not increase statistically with increased geomagnetic activity or with strong activity in the cusp, with in fact a slight tendency to decrease (Figure 4f through i). We have shown that while these facts are particularly evident for the winter cusp, similar trends exist for the whole dayside region and across seasons (Figure 2). That the trends in energy and number fluxes appear, if anything, to be decreasing rather than increasing during storm-time strongly suggests that soft precipitation is not driving the increased scintillation occurrence rates during increasingly disturbed conditions. Certainly, there are other sources that play a major role in causing ionospheric scintillations during storm-time, and some of these do not depend on particle precipitation, and might not be associated with precipitation. There is in fact a striking connection between $d\Phi/dt$ or E_{KL} and the scintillations, suggesting that we should look for parameters linked to the dynamics of the cusp.

4.1. Convection and Polar Cap Patches

There is no doubt that the dayside scintillation mostly occurs near the cusp region, as has been shown by many previous studies (Alfonsi et al., 2011; De Franceschi et al., 2019; Jin et al., 2015; Moen et al., 2013; Prikryl et al., 2015). By combining collocated GNSS scintillation receiver and all-sky imager, Jin et al. (2015) demonstrated that the dayside scintillation region is closely collocated with the active cusp auroral region for all solar wind- and IMF conditions. However, the plasma processes are highly complicated in the cusp due to the complex solar wind-magnetosphere-ionosphere coupling. This is a region where soft particles from the magnetosheath directly enter the ionosphere and cause impact ionization. The transient reconnection on the dayside magnetosphere will also impact this region through flux transfer events (FTEs, Southwood et al., 1988). The ionospheric signature of FTEs includes enhanced ionospheric flow and/or flow shears, field-aligned currents and auroral particle precipitation (Carlson, 2012; Southwood et al., 1988). Moreover, Jin et al. (2015) showed that the GNSS phase scintillations tend to occur during IMF B_Y positive. This has been explained by the intake of plasma with higher density in the afternoon sector.

In the context of a lack of change or of a decrease in energy deposition by energetic particles, there is a need to explain the enhancement in the scintillations seen when the interaction between the solar wind is felt more forcibly near its entry point at the cusp. We can think of at least two inter-related processes that can contribute to the increased scintillation activity during disturbed time: enhanced ionospheric flow and drastic density enhancements brought about by the TOI action or by polar cap patches. Upon inspection of Figure 4o, we see that scintillation events tend to occur during severe southward IMF. During such geomagnetically disturbed conditions, the area covered by the high-latitude ionospheric convection pattern expands and the flow intensifies. The expanded convection can transport high-density plasma from lower latitudes to form TOI/polar cap patches (Clausen & Moen, 2015). Compared to the density enhancements produced by soft precipitation, the density of the TOI/polar cap patches is considerably higher in the topside F region (Carlson, 2012; Clausen & Moen, 2015). Due to greater densities at F region altitudes, density structures in TOI/polar cap patches have a much longer lifetime compared to that

of precipitation induced structures, if and when the latter is created lower down where there is quicker dissipation owing to chemical recombination (Ivarsen et al., 2021a; Schunk & Sojka, 1987).

Convecting high-density plasma associated with TOI/polar cap patches provides an excellent breeding ground for plasma instabilities. For example, the growth rate of GDI is dependent both on plasma drift velocities and the steepness of plasma density gradients (Makarevich, 2017; Tsunoda, 1988). During particularly disturbed conditions, the increased flow velocity is therefore expected to create more irregularities due to GDI. In addition, the flow shears related to shears and reversed flow events can activate the shear-driven Kelvin Helmholtz Instability (KHI) (Keskinen et al., 1988; Spicher et al., 2016). KHI is thought to be more efficient in generating large- and intermediate-scale plasma gradients (Carlson, 2012; Carlson et al., 2008). In turn, then, the GDI works to break these newly created intermediate scale structures into smaller scale ones (Carlson et al., 2007). Lastly, intensified AC electric fields can induce turbulent mixing, but this effect is largely unexplored due to insufficient observations (Burston et al., 2016). We are in the process of investigating ion drift speeds in relation to observed density irregularities in a related publication.

To summarize, various localized and transient energetic dayside phenomena other than soft electrons constitute a way for particle precipitation near the cusp to influence irregularity production. PMAFs occur during dayside reconnection (Hosokawa et al., 2016), and are associated with plasma structuring (Oksavik et al., 2015). The energy transfer associated with Alfvén waves maximizes during southward IMF, and on the dayside (Billett et al., 2022; Ivarsen et al., 2020). FACs, associated with precipitating particles or Alfvén waves, can trigger the current convective instability (Ossakow & Chaturvedi, 1979). In fact, bursts of intense kilometer-scale FACs frequently occur on the dayside during elevated geomagnetic activity (Rother et al., 2007), and are associated observationally with the cusp (Lühr et al., 2004). These are some of the topics that must be investigated in future studies of cusp-associated dynamics.

4.2. Long-Term Trends in Scintillation Occurrence: A Case for Irregularity Dissipation

There is another tantalizing mechanism by which a reduction in particle precipitation will in fact facilitate the occurrence of plasma irregularities. For the cusp region, it involves ion precipitation rather than soft electron precipitation. Although the energy flux of precipitating electrons in the cusp can be orders of magnitude higher than that of ions, the entire cusp-ion energy flux will end up ionizing the E-region (Fang et al., 2013). Its effect on Pedersen conductance will be much greater than that of the soft electron flux, which typically ionizes F-region altitudes (Fang et al., 2010). In the relative absence of solar EUV photoionization (such as during local winter), the statistical decrease in ion energy flux on display in Figure 3 when the IMF B_Z becomes southward will then cause a decrease in expected Pedersen conductivity. Since Pedersen conductivity peaks in the E-region, a decrease in conductivity will translate into a decrease in the *ratio of E- to F-region conductance*, a ratio that is proportional to irregularity dissipation rates (Ivarsen et al., 2021b). This will in turn affect irregularity occurrence (Kane et al., 2012; Lamarche et al., 2020; Vickrey & Kelley, 1982).

The fact that high-latitude dissipation rates are cyclical between solstices might be an important contributor to the general seasonal trends observed in high-latitude irregularities. Illustrating this, we show in Figure 5 an analysis into how cusp-associated scintillation occurrence evolves on long timescales. First, we bin the scintillation data set by Carrington rotations, 27-day periods in which the Sun makes a full rotation (Carroll & Ostlie, 1996). We then calculate the occurrence rate of $\sigma_\phi > 0.15$ rad events over Svalbard between 10.5 and 13.5 hr MLT within each Carrington rotation. As geomagnetic activity depends to some extent on Carrington rotations, each bin will be impacted by a different dominant solar wind condition that will change from bin to bin. Some bins will have strong cusp interactions while some will not. Decay in irregularities inside each Carrington rotation, as measured from one rotation to the next will largely reflect long-term changes from rotation to rotation, in both solar EUV photoionization and geomagnetic activity.

Figure 5 plots each Carrington rotation in sequence, with scintillation occurrence rate on the *y*-axis, for the 3-years period under consideration. In solid red line we plot an empirical model that reflects both changes in geomagnetic activity and solar EUV photoionization as the 24th solar cycle approached its minimum. Appendix B derives this model (in particular, Equation B3). The declining solar cycle ensures an overall decrease in the winter occurrence rates. This decline is associated with changes in the $F_{10.7}$ solar flux, which we show in yellow hexagrams.
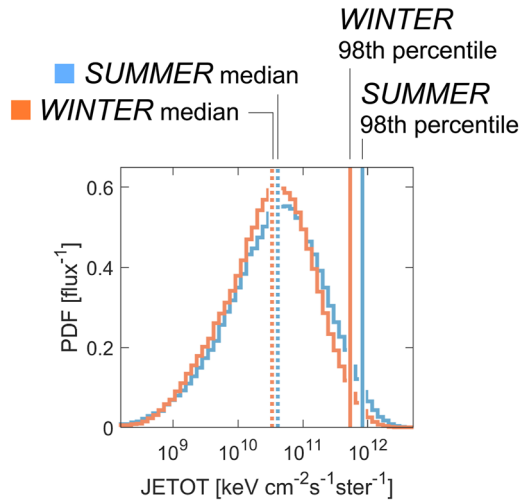
Figure 6. The distribution of cusp-associated total electron flux, for summer (blue) and winter (orange) observations, where season is again defined as a 90-days period centered on the respective solstice. The median (dashed line) and 98th percentile (solid line) values for both distributions are indicated with appropriate color.

Ionospheric conductance is affected both by the solar cycle and by the turning of the seasons, and conductance will in turn affect bulk plasma flow through basic relations between conductivity and the ionospheric electric field. The long-term effects associated with conductivity changes are thus manifold, and it is difficult at present to untangle the exact role played by irregularity dissipation rates from other conductance-related governing mechanisms. Nevertheless, Figure 5 shows clearly that whatever is driving cusp irregularity occurrence is highly dependent on season and solar cycle.

How do the seasonal changes in the cusp-associated precipitating energy flux compare? Figure 6 shows the distribution of summer (blue) and winter (orange) total integrated electron energy fluxes, in the cusp-identified DMSP measurements. The figure demonstrates that the distributions are markedly similar, with only a slight tendency for a higher energy flux during summer. It is therefore safe to say that the cusp-associated energy flux does not vary much with changing season. Nevertheless, the right-side tails of the distributions show a relatively clear seasonal contrast, with the extreme (98th percentile) values being separated appreciably. In other words, the cusp-associated energy flux maximizes during summer, opposite to that of scintillations (Figure 5). In Appendix B, we present an analysis into the seasonal trends of the 98th percentile energy flux.

4.3. Particle Precipitation and Geomagnetic Activity

We have presented the case for a quantitative evaluation of the role of cusp particle precipitation, based on the concurrent observation of increased irregularity occurrence, together with a persistent non-increase in particle precipitation. This prompted the discussion of convection and polar cap patches in Section 4.1. This being stated, the variation in cusp-associated precipitating particle energy flux with changing geomagnetic activity is of interest *in and by itself*. Why does both the ion and the electron energy flux appear to decrease with increasingly southward IMF (Figure 3)? To address this question we produced in Figure 7 a plot based on the present DMSP cusp-analysis together with measurements collected in the *dawn sector* (between 2 and 7hr MLT). The intent here is to compare cusp-precipitation to that of the early morning aurora. We therefore limited the comparison to dawn-side DMSP-observations with a total integrated energy flux exceeding 10^9 keV cm^{-2} s^{-1} ster^{-1}, which is a reasonable floor based on the data. We binned the resulting 6.2 million precipitating energy spectra by geomagnetic indices, as we had done in Figure 4. To facilitate a clear comparison between the cusp- and dawn-sectors, we now show the *percentage change* in energy flux, where 0% marks the quiet-most bin. In all five panels, the slight decrease in the cusp-associated energy flux is accompanied by an increase in the dawn-side energy flux (with the exception being positive IMF B_z, during which conditions both energy fluxes increase). In other words, an opposite trend appears between the energy flux in the cusp and dawn-side aurora.
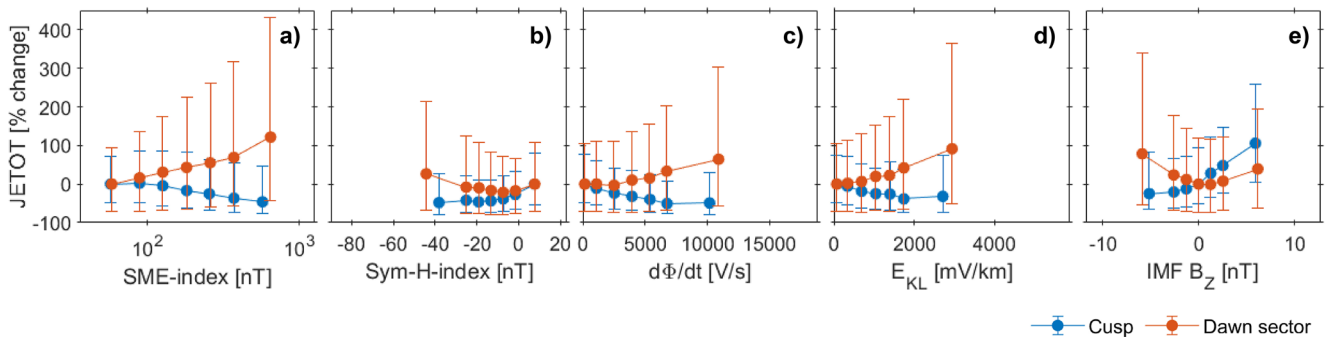

Figure 7. A similar analysis as that presented in Figure 4, comparing cusp observations (blue) to 6.2 million observations from the early morning aurora (2h < MLT < 7hr, orange). The *y*-axes show % change in each quantity from the quiet-most bin (e.g., IMF B_z = 0 nT corresponds to 0% change in panel e).

The present paper is however not the first study to point out this opposite relationship. Figures 9 and 10 in Newell et al. (2009) shows that the number flux of the "diffuse electron aurora" and ions maximize in the cusp during quiet conditions. The same two figures show unambiguously that both fluxes maximize on the nightside during disturbed geomagnetic conditions. Panel (e) of Figure 7 is thus supporting the findings in Newell et al. (2009). The authors of that paper offered an explanation for the observations of smaller precipitating fluxes for southward IMF: the low-latitude boundary layer (LLBL) is thicker during northward as opposed to southward IMF, and the LLBL is associated with particle precipitation (Ogawa et al., 2003; Yamamoto et al., 2003). Newell et al. (2009) pointed out that the rate of field-line merging at the sunward-facing magnetosphere increases during southward IMF, and this merging involves relatively cold particles. The same mechanism allows hotter particles from the magnetotail to precipitate into the nightside diffuse aurora during southward IMF, as shown in Figure 9 of Newell et al. (2009) and in Figure 7j in the present paper. This goes far in explaining the opposing trends observed between precipitation and IMF B_z in Figures 3 and 4, which could in turn provide a rudimentary explanation for all the trends we observe in the present paper: the southward IMF causes reconnection events, spurring first nightside particle precipitation, and then a drastic increase in cusp-irregularities. The latter could come through various transient phenomena associated with reconnection events, which maximize during southward IMF. That the cusp-precipitation cycle is different and in part opposite to the irregularity cycle by the changing direction of the IMF may be a key insight when unraveling what is really causing irregularity growth in the cusp ionosphere.

4.4. Extreme Events

As they frequently appear in case studies, we now briefly address the prevalence of extreme events in our data set. Figure 8 bins the data akin to Figure 3, only now binning by the SME-index, using the same seven bins as in Figure 4. However, we now plot the *distributions* of each quantity. Here, we calculate the probability density function for each distribution, as given by PDF $= c/(Nw)$, where c is the number of elements in each bin, N is the total number of elements, and w is the width of the bin (we omit y-axis information about the PDF value in order to focus only on the distribution shapes). In each panel of Figure 8 we indicate the 98th percentile value by a solid red line. We observe that as geomagnetic activity increases, the right-most tails of the scintillation distributions grows increasingly longer, and the 98th percentile value of the σ_ϕ phase scintillation index doubles. At the same time, the energy flux tails increase slightly (on both sides) throughout the SME interval. In other words, there is no clear tendency for more extreme precipitation events in the cusp with rising geomagnetic activity, as opposed to a clear tendency for more extreme scintillation events.

5. Conclusion

We analyzed a large data set of ground-based GNSS scintillation observations along with in situ precipitating particle observations. Based on a comprehensive statistical analysis of the broader dayside region (Figure 2) and the cusp (Figures 3 and 4), we have demonstrated that the cusp-associated precipitating particle energy flux decreases or stays the same during active conditions. By contrast, ionospheric irregularities in the cusp increase significantly with increasing geomagnetic activity.

Although apparently surprising, our results are broadly supported in the literature, where the seasonal and geomagnetic activity trends in precipitating energy flux and scintillations have been known to be opposite (e.g., Figure 2 in Newell et al., 2010; and Figures 2 and 4 in Prikryl et al., 2015). The result is that indices such as the SME- index, which uniquely measure the magnitude of the electrojet's Hall currents, do remarkably well in separating quiet from active conditions in the scintillations database, while not managing to parameterize the cusp energy flux in any meaningful way. (In Appendix A we show that the SME-index manages to simultaneously parameterize a southward turning of the IMF and an increase in solar wind dynamic pressure.)

The clearly observed increase in cusp-associated plasma turbulence during geomagnetically active times (Figures 4f–4j) can be said to ultimately result from an injection of free energy, followed by an accelerated return to equilibrium, a process which is broadly responsible for the observed abundance of plasma irregularities in the cusp. If particle precipitation in itself was the dominant driver of irregularities during storm-time, the energy
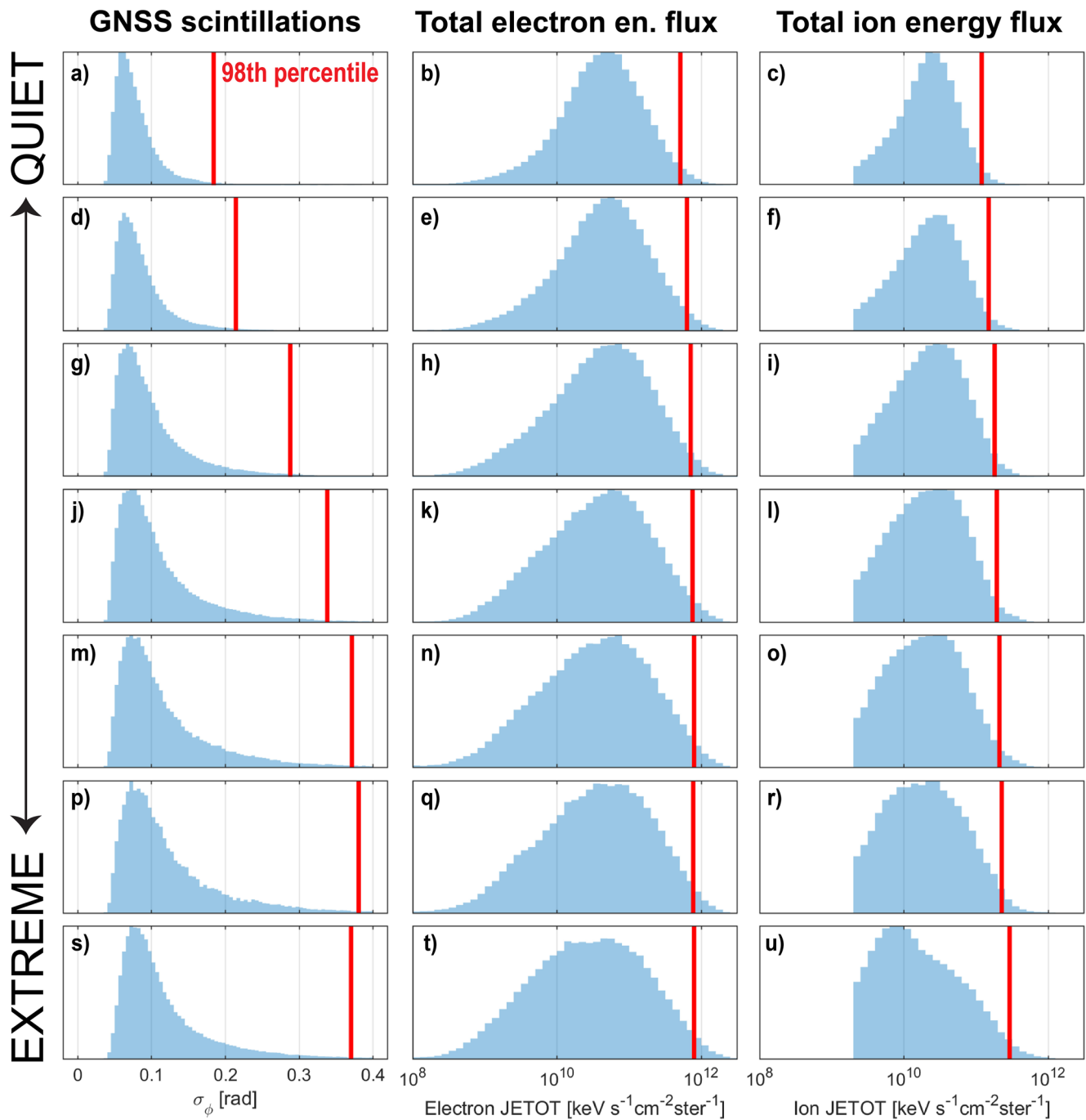
Figure 8. Distributions of phase scintillations in the cusp-region (first column), the total cusp electron energy flux (second column), and total cusp ion energy flux (third column), with separate SME-index bins for each row. The 98th percentile value is indicated in each panel with a red line. Note the sharp cutoff in the right column, which is due to the cusp definition in Newell and Meng (1988a).

flux carried by precipitating particles would in a large part be responsible for this energy injection. However, the results shown strongly suggests that the increased GNSS phase scintillation occurrence during storm-time is not driven by soft electron precipitation, and the energy pent up in the highly turbulent cusp plasma during storm-time likely has different origins.

While we proposed a range of other sources/drivers of irregularities in the cusp that could conceivably play the main role, further studies are necessary to sort them out, and thereby construct a holistic description of the cusp. We believe this is done by quantifying when and where, and under which circumstances, the different mechanisms are dominant, for example, by use of sophisticated models. Observational phenomena to consider include enhanced flow channels, Joule heating, small-scale FAC structuring, and the upwelling of the ionosphere, all of which may influence irregularity production in a variety of ways, creating an exceedingly complicated problem. Temporal variability in the cusp-associated energy flux on small timescales is likewise not accounted for in the present study.

Fortunately, the DMSP satellites are equipped with ion drift meters and magnetometers. The contribution of ionospheric flow velocity and FACs can then be evaluated with DMSP as well, and ground-based radars such as the SuperDARN network can be used to look for flow channels (Herlingshaw et al., 2019). A more comprehensive investigation into these processes will be presented in a separate study.

Appendix A: Solar Wind Conditions Parameterized by the SME-Index

An open question that has not been addressed in the present paper is why the SME-index does such a good job in separating quiet (no scintillations) from active (proliferation of scintillations) conditions in the data set. After all, the SME-index derives from hundreds of ground-based magnetometer observations at high latitudes, and is as such only measuring the magnitude of the nightside Hall currents. The SME-index is typically used to identify substorms, whereas the Sym-H-index is used to identify geomagnetic storms, two phenomena that can be related (Kamide et al., 1998). In Figure A1 we show how the IMF B_Z and B_Y components (a), the solar wind speed (b) and the solar wind dynamic pressure (c) responds to increases in the SME-index. Whereas B_Y is largely zero-valued (or consistent with zero) for all values of the SME-index, the B_Z component shows a clear preference for being positive during low SME and being negative for high SME. Likewise, both the wind speed and dynamic pressure show a clear increase with increasing SME-index. Though the spread (error bars) is high throughout Figure A1, the trends are clear. During times of elevated nightside activity, the solar wind is effectively pushing against the magnetosphere-ionosphere system. Observationally, we conclude that the SME-index parameterizes a southward turning of the IMF and increased dynamic pressure simultaneously.
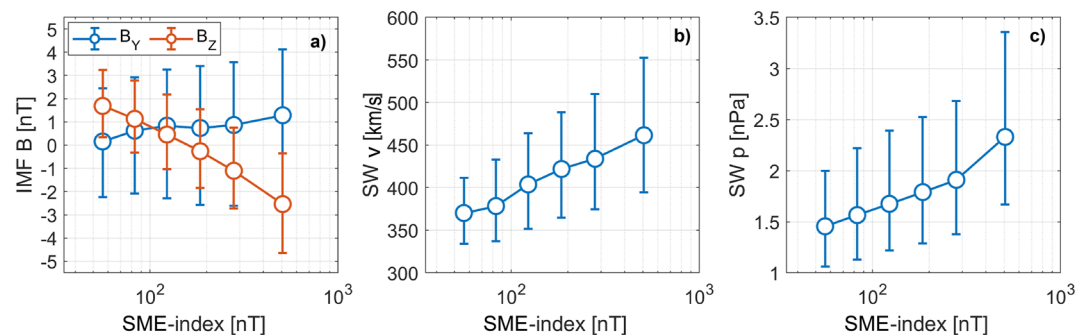

Figure A1. Solar wind conditions from OMNI (1-min data smoothed with a 30-min median filter), binned by SME-index for the period between 2014 and 2016. Errorbars denote upper/lower quartile distributions.

Appendix B: Solar Zenith Angle Deconstruction: An Empirical Model

In Section 4.2, we presented Figure 5, which shows the long-term evolution of cusp-associated scintillation events. The solid red line in that figure represents an empirical model designed to capture both seasonal and solar cycle-associated trends in the data. That model, which we dub Solar Zenith Angle Deconstruction, is obtained by a linear fit of scintillation occurrence against solar zenith angle, with solar cycle-based trends.

First, we construct a slowly evolving solar cycle trend,

$$\Gamma_{SC}(t) = \Gamma_0 + \frac{3\sigma}{2} e^{(t-t_0)^2/4\tau_1^2}, \tag{B1}$$

where t is the number of days since 0 January year 0. Equation B1 then consists of a Gaussian function over a baseline ($\Gamma_0 = 3\%$), with t_0 being the previous solar cycle peak in April 2014, and $\tau_1 = 1.3$ years, parameters obtained by trial and error (self-justified as evident in Figure 5). The Gaussian is scaled by a fraction of σ, the standard deviation of all occurrence rates in 2014–2016.

Next, we subtract that model from the long-term data, yielding a detrended long-term scintillation occurrence rate, for each Carrington rotation in the dataset. In Figure B1 we plot each Carrington rotation against the mean solar zenith angle (adjusted for an altitude of 350 km) in each bin; here we distinguish between bins that occur before June 2015 (red) and after June 2015 (green), for reasons that will soon become clear.

In Figure B1, solid red and green lines shows a linear fit of de-trended occurrence rates versus solar zenith angle,

$$\Gamma_{SZA}(z, t) = (a + b z)e^{-(t-t_0)/\tau_2}, \tag{B2}$$

where z represents solar zenith angle in degrees. The parameters $a = -29\%$ and $b = 0.38\%/°$ fits the red data well. The exponent represents the solar cycle-related damping term controlled by the characteristic timescale $\tau_2 = 2.5$ years. The solid red line in Figure B1 plots Equation B2 with no damping, while a green line plots Equation B2 with 60% damping, representing conditions that approach solar minimum. Lastly, we identify in yellow five bins that are both sparse in irregularity occurrence and largely recorded in darkness. These bins
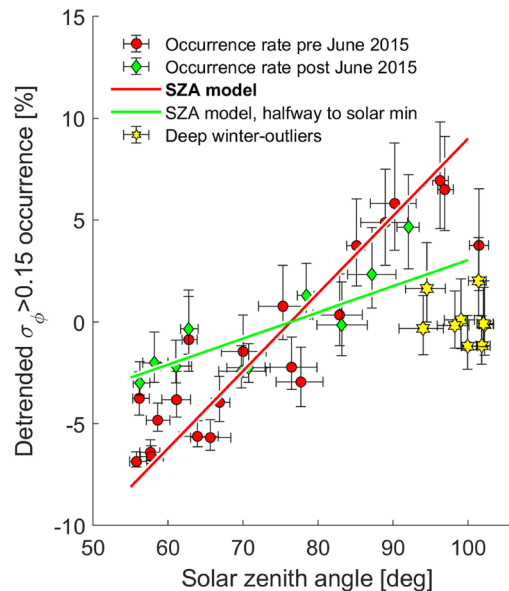

Figure B1. The occurrence rate of scintillation events in the cusp-region, binned by Carrington rotations (27-day periods of solar rotation), for 10.5 hr < MLT < 13.5 hr MLT over Svalbard. Red and green colors denote data collected before and after June 2015 respectively. The figure plots de-trended data against solar zenith angle (de-trended by subtracting Equation B1), and includes a linear fit for solar maximum conditions (Equation B2) in solid red, with a green line showing that equation evaluated halfway to solar minimum. Yellow datapoints belong to a deep-winter outlier group. Solar zenith angles are adjusted for the expected ionospheric piercing point altitudes, so that a zenith angle of 90° denotes the solar terminator at an altitude of 350 km.

occur during deep winter, and feature exceedingly low plasma densities (Jin et al., 2018), to the extent that irregularity amplitudes are simply too low to excite scintillations. For clarity, these bins are removed from Figure 5.

Finally, we are in a position to write out the composite empirical model (solid red line in Figure 5). That is, Equation B1 + Equation B2,

$$\hat{\Gamma}(t) = \Gamma_0 + \frac{3\sigma}{2} e^{(t-t_0)^2/4\tau_1^2} + [a + b\,z(t)]e^{-(t-t_0)/\tau_2}.$$ (B3)

What follows is a justification and a description of this composite model, where we also refer to the discussion in Section 4.2. First, the solar cycle term (Equation B1) ensures a steady decrease in occurrence rate during the declining phase of the 24th solar cycle. But the data also favors a decrease in annual variation. The linear solar zenith angle-model (Equation B2) represents an expected direct relation between solar illumination (solar zenith angle) and dissipation rates and effective growth rates (Ivarsen et al., 2019). Since the zenith angle is a geometric quantity, its variation is perfectly cyclical with season, and so must be dampened to reflect the observed decreasing annual variation. With all three factors considered, Equation B3 captures the competing effect of a declining winter-occurrence rate and a slightly rising summer-occurrence rate. Except for the deep-winter outliers (yellow hexagrams in Figure B1), the composite model Equation B3 fits the irregularity occurrence data well, both in terms of seasonal fluctuations and solar cycle trend. We thus see tentative evidence that the discussion of irregularity dissipation in Section 4.2 accurately describes long-term trends in cusp-associated plasma irregularities.

Lastly, we must briefly discuss the significance of the decay rate τ_2 in Equation B2, the long-term model used as a fit to the cusp-region scintillations in Figure 5. There, a decay-rate of 2.5 years, coupled with the slowly decaying baseline trend (Equation B1), adequately describes the data. The former implies that the variation in cusp irregularity occurrence rates would experience an e-fold decrease every 2 years after the solar cycle peak. Together with the decreasing baseline (the solar cycle term), the two timescales quantify the decay in expected maximum scintillation occurrence rate in the cusp during any given Carrington rotation period. This involves considering the damping term τ_2 in Equation B2 as a characteristic decay parameter, and Equation B3 as a novel way to consider plasma irregularity "lifetimes" on ultra-long timescales. Figure B2 shows the maximum (red) and minimum (blue) permitted annual occurrence rate within the model Equation B3, obtained by plotting that equation with maximum and minimum possible annual variation respectively. We validate the solar cycle-trends with the occurrence rates for an extended timeperiod, including data up until 2018. The long-term decay present in the red line, which is supported by the extended data set, shows a characteristic lifetime, and documents how the landscape of northern hemisphere cusp
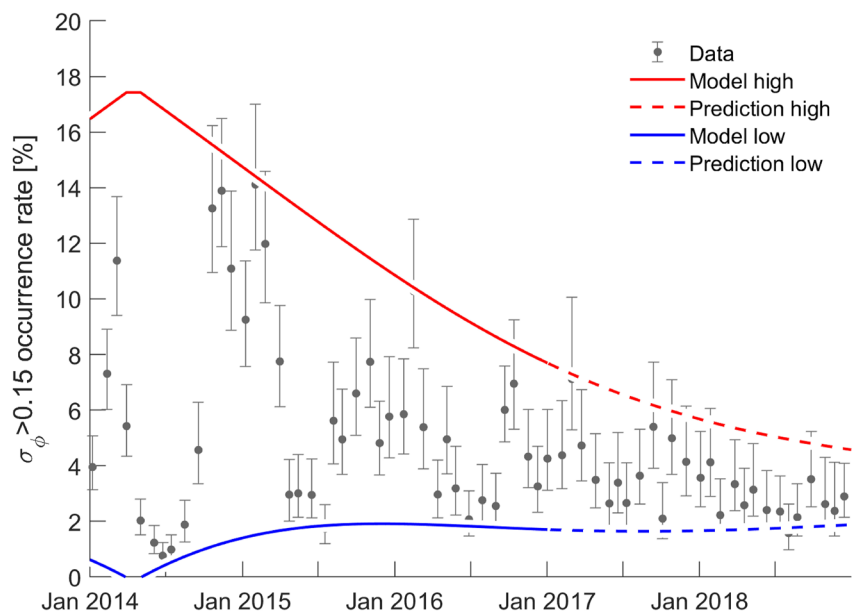

Figure B2. All Carrington rotations for the extended period 2014–2018 plotted in sequence (dark gray circles). The red and blue lines show Equation B3 with maximum and minimum solar zenith angle variation inserted *in lieu* of the *z*-dependent term respectively. Solid line shows the model validity, while dashed lines make a prediction for the years 2017 and 2018.

plasma irregularities tended to decrease in severity as the solar cycle 24 progressed toward a minimum. The decrease is strong—the winter occurrence rates decline from around 15% during the solar cycle peak to around 5% near the minimum. This decay, or characteristic lifetime, finds support in a recent study by Lovati et al. (2023), where the authors discuss this decline in relation to the F10.7 solar flux (see Figure 6 in that paper, and Figure 5 in the present paper). Note that the time-period analyzed here is short, and so we cannot draw conclusions on general solar cycle trends. The results are primarily valid for the descending phase of Solar Cycle 24.

B1. Application to the the Cusp Energy Flux

Published climatologies document seasonal trends in dayside precipitation (Newell et al., 2010). However, we are not aware of analyses into the seasonal trends in precipitation that is directly associated with the cusp, and so we shall present such an analysis here by application of the above empirical model to the 98th percentile cusp-associated energy flux, in which quantity there is an appreciably seasonal contrast (see Figure 6). The relevance of the 98th percentile energy flux is heightened by Figure 8, which is concerned with extreme events in our two databases. We can then address the question of whether extreme precipitation events are more common during local winter, when scintillation events tend to occur.

Figure B3 shows a similar analysis to that of Figures 5 and B1: we bin the DMSP cusp-associated energy flux by Carrington rotations, taking the 98th percentile energy flux for each rotation. Low- and high-vertical errorbars now denote the 97th and 99th percentile flux respectively. As geomagnetic activity is often somewhat cyclical in Carrington rotations, the 98th percentile energy flux is a good measure of the extreme flux events in each consecutive solar rotation. In Figure B3a, we subtract a solar cycle trend,

$$\Phi_{SC}(t) = \Phi_0 + \frac{\sigma}{2} e^{(t-t_0)^2/4\tau_1^2}, \tag{B4}$$

where Φ denotes the 98th percentile total energy flux. τ_1 is unchanged from Equation B1, but the standard deviation σ is now halved. We then calculate a linear fit, but now with an *intensifying* term as the solar cycle progresses,

$$\Phi_{SZA}(z, t) = (a + b\,z)e^{+(t-t_0)/\tau_3}, \tag{B5}$$

Seasonal trends in the cusp 98th percentile energy flux
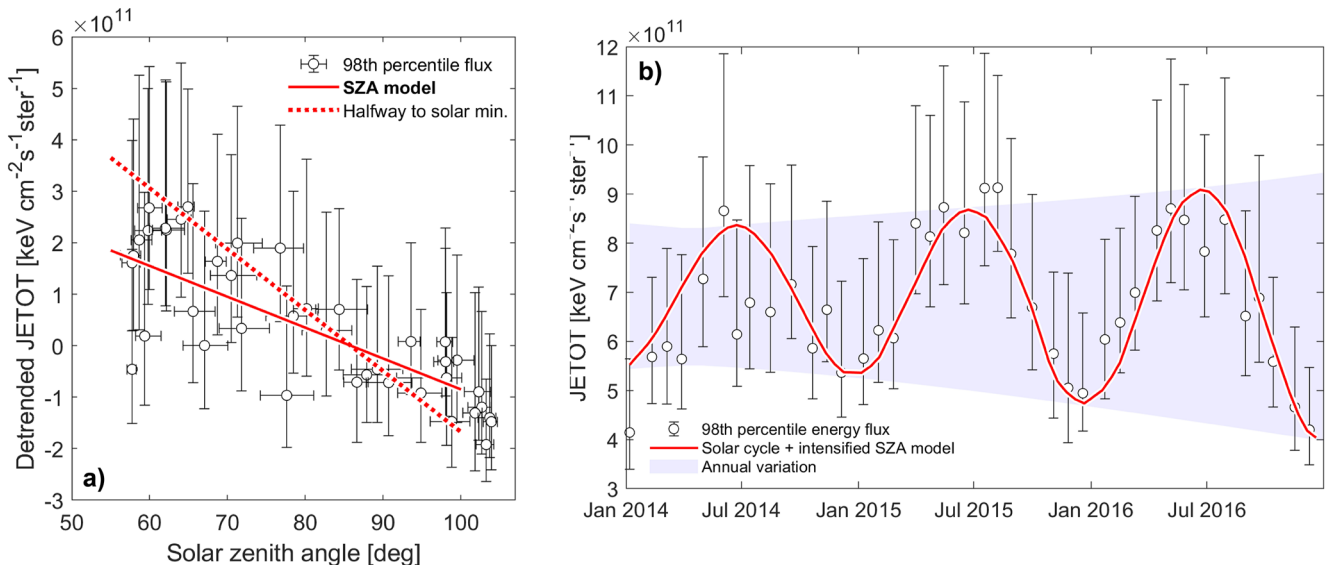

Figure B3. The 98th percentile total energy flux in the cusp-measured DMSP datapoints, binned by Carrington rotations. Panel (a) shows the 98th percentile energy flux in each 27-days solar rotation period, with low- and high-errorbars showing the location of the 97th and 99th percentile flux respectively. A solar zenith angle deconstruction model (Equation B5) is shown in solid red line, but now with an intensification (dashed red line) halfway to solar minimum. Panel (b) shows the energy flux bins in sequence, with the composite model (Equation B4 + Equation B5) in solid red line, and with annual variation during the solar cycle declining phase in shaded light blue area.

where $\tau_3 = 4$ years, and the exponent is positive, meaning that the variation in the 98th percentile energy flux undergoes an *e*-fold *increase* after 4 years into the declining phase of solar cycle 24. The dashed red line in Figure B3a shows the fit evaluated at the end of 2016, when the intensifying term has reached the value 2 (a doubling). Finally, panel (b) shows the Carrington rotation bins in sequence, with the composite fit (Equation B4 + Equation B5) in a solid red line, and total annual variation as a function of solar cycle in shaded light-blue area.

First we note that there is considerable spread. The distributions in both panels are almost consistent with the solid red lines being flat, as is hinted at in Figure 6, where the distributions are markedly similar. Nevertheless, the tendency for a seasonal dependency is there: extreme precipitation events go through a maximum in energy flux during summer. On top of that, as is shown by the dashed red line in panel (a) and the shaded blue region in panel (b), extreme flux events in the cusp exhibit *larger* annual variability toward the solar cycle minimum. The seasonal and 24th solar cycle-trends in cusp-associated electron energy flux are then opposite compared to those of scintillation occurrence rates (Figure 5), and in line with the "dayside diffuse electrons" (Newell et al., 2009, 2010).

Data Availability Statement

SuperMAG data can be accessed at https://supermag.jhuapl.edu/mag/. Precipitating particle data from DMSP SSJ can be accessed through Madrigal (http://cedar.openmadrigal.org/). GNSS scintillation data from Svalbard are organized with the following nine DOIs. Receiver at Bjørnøya: https://doi.org/10.18710/CMZEWF (2014), https://doi.org/10.18710/QG9XCM (2015), https://doi.org/10.18710/BPU1RV (2016). Kjell Henriksen receiver: https://doi.org/10.18710/LZX3MU (2014), https://doi.org/10.18710/13FHF9 (2015), https://doi.org/10.18710/1CA1KO (2016). Receiver at Ny Ålesund: https://doi.org/10.18710/P69VFS (2014), https://doi.org/10.18710/MIUYBH (2015), https://doi.org/10.18710/D46B20 (2016). Interplanetary magnetic field observations and various geomagnetic indices from NASA's OMNI service can be accessed at https://omniweb.gsfc.nasa.gov/.

References

Aarons, J., Mullen, J. P., Whitney, H. E., Johnson, A. L., & Weber, E. J. (1981). UHF scintillation activity over polar latitudes. *Geophysical Research Letters*, *8*(3), 277–280. https://doi.org/10.1029/GL008i003p00277

Alfonsi, L., Spogli, L., De Franceschi, G., Romano, V., Aquino, M., Dodson, A., & Mitchell, C. N. (2011). Bipolar climatology of GPS ionospheric scintillation at solar minimum. *Radio Science*, *46*(3). https://doi.org/10.1029/2010RS004571

Baker, K. B., & Wing, S. (1989). A new magnetic coordinate system for conjugate studies at high latitudes. *Journal of Geophysical Research*, *94*(A7), 9139–9143. https://doi.org/10.1029/JA094iA07p09139

Basu, S., Basu, S., MacKenzie, E., Coley, W. R., Sharber, J. R., & Hoegy, W. R. (1990). Plasma structuring by the gradient drift instability at high latitudes and comparison with velocity shear driven processes. *Journal of Geophysical Research*, *95*(A6), 7799–7818. https://doi.org/10.1029/JA095iA06p07799

Bell, P. M. (1981). Magnetospheric cleft. *EOS Transactions*, *62*(52), 1201. https://doi.org/10.1029/EO062i052p01201-02

Billett, D. D., McWilliams, K. A., Pakhotin, I. P., Burchill, J. K., Knudsen, D. J., & Martin, C. J. (2022). High-resolution poynting flux statistics from the swarm mission: How much is being underestimated at larger scales? *Journal of Geophysical Research: Space Physics*, *127*(7), e2022JA030573. https://doi.org/10.1029/2022JA030573

Brekke, A., & Moen, J. (1993). Observations of high latitude ionospheric conductances. *Journal of Atmospheric and Terrestrial Physics*, *55*(11), 1493–1512. https://doi.org/10.1016/0021-9169(93)90126-J

Burston, R., Mitchell, C., & Astin, I. (2016). A comparison of the relative effect of the Earth's quasi-DC and AC electric field on gradient drift waves in large-scale plasma structures in the polar regions. *Journal of Geophysical Research: Space Physics*, *121*(9), 9012–9019. https://doi.org/10.1002/2016JA022676

Carlson, H. C. (2012). Sharpening our thinking about polar cap ionospheric patch morphology, research, and mitigation techniques. *Radio Science*, *47*(4). https://doi.org/10.1029/2011RS004946

Carlson, H. C., Oksavik, K., & Moen, J. (2008). On a new process for cusp irregularity production. *Annales Geophysicae*, *26*(9), 2871–2885. https://doi.org/10.5194/angeo-26-2871-2008

Carlson, H. C., Pedersen, T., Basu, S., Keskinen, M., & Moen, J. (2007). Case for a new process, not mechanism, for cusp irregularity production. *Journal of Geophysical Research*, *112*(A11), A11304. https://doi.org/10.1029/2007JA012384

Carroll, B. W., & Ostlie, D. A. (1996). *An introduction to modern astrophysics*. Addison-Wesley.

Clausen, L. B. N., & Moen, J. I. (2015). Electron density enhancements in the polar cap during periods of dayside reconnection. *Journal of Geophysical Research: Space Physics*, *120*(6), 4452–4464. https://doi.org/10.1002/2015JA021188

Cowley, S. W. H. (2000). TUTORIAL: Magnetosphere-ionosphere interactions: A tutorial review. In *Washington DC American geophysical union geophysical monograph series* (Vol. 118, p. 91). https://doi.org/10.1029/GM118p0091

Crowley, G. (1996). Critical review of ionospheric patches and blobs. *Review of Radio Science*, 619–648.

De Franceschi, G., Spogli, L., Alfonsi, L., Romano, V., Cesaroni, C., & Hunstad, I. (2019). The ionospheric irregularities climatology over Svalbard from solar cycle 23. *Scientific Reports*, *9*(1), 9232. https://doi.org/10.1038/s41598-019-44829-5

Dyson, P. L., McClure, J. P., & Hanson, W. B. (1974). In situ measurements of the spectral characteristics of F region ionospheric irregularities. *Journal of Geophysical Research*, *79*(10), 1497–1502. https://doi.org/10.1029/JA079i010p01497

Fang, X., Lummerzheim, D., & Jackman, C. H. (2013). Proton impact ionization and a fast calculation method. *Journal of Geophysical Research: Space Physics*, *118*(8), 5369–5378. https://doi.org/10.1002/jgra.50484

Fang, X., Randall, C. E., Lummerzheim, D., Wang, W., Lu, G., Solomon, S. C., & Frahm, R. A. (2010). Parameterization of monoenergetic electron impact ionization. *Geophysical Research Letters*, *37*(22), L22106. https://doi.org/10.1029/2010GL045406

Frederick-Frost, K. M., Lynch, K. A., Kintner, P. M., Jr., Klatt, E., Lorentzen, D., Moen, J., et al. (2007). SERSIO: Svalbard EISCAT rocket study of ion outflows. *Journal of Geophysical Research*, *112*(A8), A08307. https://doi.org/10.1029/2006JA011942

Gjerloev, J. W. (2012). The SuperMAG data processing technique. *Journal of Geophysical Research*, *117*(A9), A09213. https://doi.org/10.1029/2012JA017683

Goodwin, L., Iserhienrhien, B., Miles, D. M., Patra, S., van der Meeren, C., Buchert, S. C., et al. (2015). Swarm in situ observations of F region polar cap patches created by cusp precipitation. *Geophysical Research Letters*, *42*(4), 996–1003. https://doi.org/10.1002/2014GL062610

Hamza, A. M., Song, K., Meziane, K., & Thayyil, J. P. (2023). Two-component phase scintillation spectra in the auroral region: Observations and Model. ESSOAR preprint repository. https://doi.org/10.22541/essoar.169272227.79637429/v1

Herlingshaw, K., Baddeley, L. J., Oksavik, K., Lorentzen, D. A., & Bland, E. C. (2019). A study of automatically detected flow channels in the polar cap ionosphere. *Journal of Geophysical Research*, *124*(11), 9430–9447. https://doi.org/10.1029/2019JA026916

Hosokawa, K., Taguchi, S., & Ogawa, Y. (2016). Periodic creation of polar cap patches from auroral transients in the cusp. *Journal of Geophysical Research: Space Physics*, *121*(6), 5639–5652. https://doi.org/10.1002/2015JA022221

Ivarsen, M. F., Jin, Y., Spicher, A., & Clausen, L. B. N. (2019). Direct evidence for the dissipation of small-scale ionospheric plasma structures by a conductive E region. *Journal of Geophysical Research: Space Physics*, *124*(4), 2935–2942. https://doi.org/10.1029/2019JA026500

Ivarsen, M. F., Jin, Y., Spicher, A., Miloch, W., & Clausen, L. B. N. (2021a). The lifetimes of plasma structures at high latitudes. *Journal of Geophysical Research: Space Physics*, *126*(2), e2020JA028117. https://doi.org/10.1029/2020JA028117

Ivarsen, M. F., Park, J., Kwak, Y.-S., Jin, Y., Knudsen, D. J., & Clausen, L. B. N. (2020). Observational evidence for the role of hall conductance in Alfvén wave reflection. *Journal of Geophysical Research: Space Physics*, *125*(12), e2020JA028119. https://doi.org/10.1029/2020JA028119

Ivarsen, M. F., St-Maurice, J.-P., Jin, Y., Park, J., Miloch, W., Spicher, A., et al. (2021b). Steepening plasma density spectra in the ionosphere: The crucial role played by a strong E-region. *Journal of Geophysical Research: Space Physics*, *126*(8), e2021JA029401. https://doi.org/10.1029/2021JA029401

Jin, Y., Miloch, W. J., Moen, J. I., & Clausen, L. B. N. (2018). Solar cycle and seasonal variations of the GPS phase scintillation at high latitudes. *Journal of Space Weather and Space Climate*, *8*, A48. https://doi.org/10.1051/swsc/2018034

Jin, Y., Moen, J. I., & Miloch, W. J. (2014). GPS scintillation effects associated with polar cap patches and substorm auroral activity: Direct comparison. *Journal of Space Weather and Space Climate*, *4*, A23. https://doi.org/10.1051/swsc/2014019

Jin, Y., Moen, J. I., & Miloch, W. J. (2015). On the collocation of the cusp aurora and the GPS phase scintillation: A statistical study. *Journal of Geophysical Research: Space Physics*, *120*(10), 9176–9191. https://doi.org/10.1002/2015JA021449

Jin, Y., Moen, J. I., Oksavik, K., Spicher, A., Clausen, L. B. N., & Miloch, W. J. (2017). GPS scintillations associated with cusp dynamics and polar cap patches. *Journal of Space Weather and Space Climate*, *7*, A23. https://doi.org/10.1051/swsc/2017022

Jin, Y., Moen, J. I., Spicher, A., Oksavik, K., Miloch, W. J., Clausen, L. B. N., et al. (2019). Simultaneous rocket and scintillation observations of plasma irregularities associated with a reversed flow event in the cusp ionosphere. *Journal of Geophysical Research: Space Physics*, *124*(8), 7098–7111. https://doi.org/10.1029/2019JA026942

Kamide, Y., Baumjohann, W., Daglis, I. A., Gonzalez, W. D., Grande, M., Joselyn, J. A., et al. (1998). Current understanding of magnetic storms: Storm-substorm relationships. *Journal of Geophysical Research*, *103*(A8), 17705–17728. https://doi.org/10.1029/98JA01426

Kan, J. R., & Lee, L. C. (1979). Energy coupling function and solar wind-magnetosphere dynamo. *Geophysical Research Letters*, *6*(7), 577–580. https://doi.org/10.1029/GL006i007p00577

Kane, T. A., Makarevich, R. A., & Devlin, J. C. (2012). HF radar observations of ionospheric backscatter during geomagnetically quiet periods. *Annales Geophysicae*, *30*(1), 221–233. https://doi.org/10.5194/angeo-30-221-2012

Kelley, M. C., Vickrey, J. F., Carlson, C. W., & Torbert, R. (1982). On the origin and spatial extent of high-latitude F region irregularities. *Journal of Geophysical Research*, *87*(A6), 4469–4475. https://doi.org/10.1029/JA087iA06p04469

Keskinen, M. J., Mitchell, H. G., Fedder, J. A., Satyanarayana, P., & Zalesak, S. T. (1988). *Nonlinear evolution of the Kelvin-Helmholtz instability in the high latitude ionosphere*. (Technical Report No. NRL-MR-6043). Naval Research Lab Washington DC. Retrieved from http://www.dtic.mil/docs/citations/ADA188875

Kintner, P. M., Ledvina, B. M., & de Paula, E. R. (2007). GPS and ionospheric scintillations. *Space Weather*, *5*(9). https://doi.org/10.1029/2006SW000260

Lamarche, L. J., Varney, R. H., & Siefring, C. L. (2020). Analysis of plasma irregularities on a range of scintillation-scales using the resolute bay incoherent scatter radars. *Journal of Geophysical Research: Space Physics*, *125*(3), e2019JA027112. https://doi.org/10.1029/2019JA027112

Li, K., Haaland, S., Eriksson, A., André, M., Engwall, E., Wei, Y., et al. (2012). On the ionospheric source region of cold ion outflow. *Geophysical Research Letters*, *39*(18), L18102. https://doi.org/10.1029/2012GL053297

Liou, K., Newell, P. T., & Meng, C.-I. (2001). Seasonal effects on auroral particle acceleration and precipitation. *Journal of Geophysical Research*, *106*(A4), 5531–5542. https://doi.org/10.1029/1999JA000391

Lockwood, M., & Carlson, H. C., Jr. (1992). Production of polar cap electron density patches by transient magnetopause reconnection. *Geophysical Research Letters*, *19*(17), 1731–1734. https://doi.org/10.1029/92GL01993

Lovati, G., De Michelis, P., Consolini, G., Pezzopane, M., Pignalberi, A., & Berrilli, F. (2023). Decomposing solar and geomagnetic activity and seasonal dependencies to examine the relationship between GPS loss of lock and ionospheric turbulence. *Scientific Reports*, *13*(1), 9287. https://doi.org/10.1038/s41598-023-34727-2

Lühr, H., Rother, M., Köhler, W., Ritter, P., & Grunwaldt, L. (2004). Thermospheric up-welling in the cusp region: Evidence from CHAMP observations. *Geophysical Research Letters*, *31*(6), L06805. https://doi.org/10.1029/2003GL019314

Makarevich, R. A. (2017). Critical density gradients for small-scale plasma irregularity generation in the E and F regions. *Journal of Geophysical Research: Space Physics*, *122*(9), 9588–9602. https://doi.org/10.1002/2017JA024393

Meziane, K., Hamza, A. M., & Jayachandran, P. T. (2023). Turbulence signatures in high-latitude ionospheric scintillation. *Journal of Geophysical Research: Space Physics*, *128*(1), e2022JA030934. https://doi.org/10.1029/2022JA030934

Mitchell, C. N., Alfonsi, L., De Franceschi, G., Lester, M., Romano, V., & Wernik, A. W. (2005). GPS TEC and scintillation measurements from the polar ionosphere during the October 2003 storm. *Geophysical Research Letters*, *32*(12), L12S03. https://doi.org/10.1029/2004GL021644

Moen, J., Oksavik, K., Abe, T., Lester, M., Saito, Y., Bekkeng, T. A., & Jacobsen, K. S. (2012). First in-situ measurements of HF radar echoing targets. *Geophysical Research Letters*, *39*(7), L07104. https://doi.org/10.1029/2012GL051407

Moen, J., Oksavik, K., Alfonsi, L., Daabakk, Y., Romano, V., & Spogli, L. (2013). Space weather challenges of the polar cap ionosphere. *Journal of Space Weather and Space Climate*, *3*, A02. https://doi.org/10.1051/swsc/2013025

Moen, J., Walker, I. K., Kersley, L., & Milan, S. E. (2002). On the generation of cusp HF backscatter irregularities. *Journal of Geophysical Research*, *107*(A4), SIA3–1–SIA3–5. https://doi.org/10.1029/2001JA000111

Newell, P. T., & Gjerloev, J. W. (2011). Evaluation of SuperMAG auroral electrojet indices as indicators of substorms and auroral power. *Journal of Geophysical Research*, *116*(A12), A12211. https://doi.org/10.1029/2011JA016779

Newell, P. T., & Meng, C.-I. (1988a). The cusp and the cleft/boundary layer: Low-altitude identification and statistical local time variation. *Journal of Geophysical Research*, *93*(A12), 14549–14556. https://doi.org/10.1029/JA093iA12p14549

Newell, P. T., & Meng, C.-I. (1988b). Hemispherical asymmetry in cusp precipitation near solstices. *Journal of Geophysical Research*, *93*(A4), 2643–2648. https://doi.org/10.1029/JA093iA04p02643

Newell, P. T., Sotirelis, T., Liou, K., Meng, C.-I., & Rich, F. J. (2007). A nearly universal solar wind-magnetosphere coupling function inferred from 10 magnetospheric state variables. *Journal of Geophysical Research*, *112*(A1), A01206. https://doi.org/10.1029/2006JA012015

Newell, P. T., Sotirelis, T., & Wing, S. (2009). Diffuse, monoenergetic, and broadband aurora: The global precipitation budget. *Journal of Geophysical Research*, *114*(A9), A09207. https://doi.org/10.1029/2009JA014326

Newell, P. T., Sotirelis, T., & Wing, S. (2010). Seasonal variations in diffuse, monoenergetic, and broadband aurora. *Journal of Geophysical Research*, *115*(A3), A03216. https://doi.org/10.1029/2009JA014805

Ogawa, Y., Fujii, R., Buchert, S. C., Nozawa, S., & Ohtani, S. (2003). Simultaneous EISCAT Svalbard radar and DMSP observations of ion upflow in the dayside polar ionosphere. *Journal of Geophysical Research*, *108*(A3), 1101. https://doi.org/10.1029/2002JA009590

Oksavik, K. (2020). *The university of Bergen global navigation satellite system data collection*. DataverseNO. https://doi.org/10.18710/AJ4S-X394

Oksavik, K., van der Meeren, C., Lorentzen, D. A., Baddeley, L. J., & Moen, J. (2015). Scintillation and loss of signal lock from poleward moving auroral forms in the cusp ionosphere. *Journal of Geophysical Research: Space Physics*, *120*(10), 9161–9175. https://doi.org/10.1002/2015JA021528

Ossakow, S. L., & Chaturvedi, P. K. (1979). Current convective instability in the diffuse aurora. *Geophysical Research Letters*, *6*(4), 332–334. https://doi.org/10.1029/GL006i004p00332

Papitashvili, N. E., & King, J. H. (2020). *OMNI hourly data set*. NASA Space Physics Data Facility. https://doi.org/10.48322/1SHR-HT18

Prikryl, P., Jayachandran, P. T., Chadwick, R., & Kelly, T. D. (2015). Climatology of GPS phase scintillation at northern high latitudes for the period from 2008 to 2013. *Annales Geophysicae*, *33*(5), 531–545. https://doi.org/10.5194/angeo-33-531-2015

Redmon, R. J., Denig, W. F., Kilcommons, L. M., & Knipp, D. J. (2017). New DMSP database of precipitating auroral electrons and ions. *Journal of Geophysical Research: Space Physics*, *122*(8), 9056–9067. https://doi.org/10.1002/2016JA023339

Rother, M., Schlegel, K., & Lühr, H. (2007). CHAMP observation of intense kilometer-scale field-aligned currents, evidence for an ionospheric Alfvén resonator. *Annales Geophysicae*, *25*(7), 1603–1615. https://doi.org/10.5194/angeo-25-1603-2007

Sandholt, P. E., Deehr, C. S., Egeland, A., Lybekk, B., Viereck, R., & Romick, G. J. (1986). Signatures in the dayside aurora of plasma transfer from the magnetosheath. *Journal of Geophysical Research*, *91*(A9), 10063–10079. https://doi.org/10.1029/JA091iA09p10063

Sandholt, P. E., Farrugia, C. J., Moen, J., Noraberg, O., Lybekk, B., Sten, T., & Hansen, T. (1998). A classification of dayside auroral forms and activities as a function of interplanetary magnetic field orientation. *Journal of Geophysical Research*, *103*(A10), 23325–23345. https://doi.org/10.1029/98JA02156

Saunders, M. (1989). The polar cusp ionosphere: A window on solar wind–magnetosphere coupling. *Antarctic Science*, *1*(3), 193–203. https://doi.org/10.1017/S0954102089000313

Schunk, R. W., & Sojka, J. J. (1987). A theoretical study of the lifetime and transport of large ionospheric density structures. *Journal of Geophysical Research*, *92*(A11), 12343–12351. https://doi.org/10.1029/JA092iA11p12343

Shepherd, G. G. (1979). Dayside cleft aurora and its ionospheric effects. *Reviews of Geophysics*, *17*(8), 2017–2033. https://doi.org/10.1029/RG017i008p02017

Song, K., Hamza, A. M., Jayachandran, P. T., Meziane, K., & Kashcheyev, A. (2023). Spectral characteristics of phase fluctuations at high latitude. *Journal of Geophysical Research: Space Physics*, *128*(9), e2022JA031244. https://doi.org/10.1029/2022JA031244

Southwood, D. J., Farrugia, C. J., & Saunders, M. A. (1988). What are flux transfer events? *Planetary and Space Science*, *36*(5), 503–508. https://doi.org/10.1016/0032-0633(88)90109-2

Spicher, A., Deshpande, K., Jin, Y., Oksavik, K., Zettergren, M. D., Clausen, L. B. N., et al. (2020). On the production of ionospheric irregularities via Kelvin-Helmholtz instability associated with cusp flow channels. *Journal of Geophysical Research: Space Physics*, *125*(6), e2019JA027734. https://doi.org/10.1029/2019JA027734

Spicher, A., Ilyasov, A. A., Miloch, W. J., Chernyshov, A. A., Clausen, L. B. N., Moen, J. I., et al. (2016). Reverse flow events and small-scale effects in the cusp ionosphere. *Journal of Geophysical Research: Space Physics*, *121*(10), 10466–10480. https://doi.org/10.1002/2016JA022999

Spicher, A., Miloch, W. J., Clausen, L. B. N., & Moen, J. I. (2015). Plasma turbulence and coherent structures in the polar cap observed by the ICI-2 sounding rocket. *Journal of Geophysical Research: Space Physics*, *120*(12), 2015JA021634. https://doi.org/10.1002/2015JA021634

Spogli, L., Alfonsi, L., De Franceschi, G., Romano, V., Aquino, M. H. O., & Dodson, A. (2010). Climatology of GNPs ionospheric scintillation at high and mid latitudes under different solar activity conditions. *Nuovo Cimento. B*, *125*. Retrieved from https://www.osti.gov/etdeweb/biblio/21466092

Spogli, L., Alfonsi, L., Romano, V., De Franceschi, G., Joao Francisco, G. M., Hirokazu Shimabukuro, M., et al. (2013). Assessing the GNSS scintillation climate over Brazil under increasing solar activity. *Journal of Atmospheric and Solar-Terrestrial Physics*, *105*, 199–206. https://doi.org/10.1016/j.jastp.2013.10.003

Titheridge, J. E. (1976). Ionospheric heating beneath the magnetospheric cleft. *Journal of Geophysical Research*, *81*(19), 3221–3226. https://doi.org/10.1029/JA081i019p03221

Tsunoda, R. T. (1988). High-latitude F region irregularities: A review and synthesis. *Reviews of Geophysics*, *26*(4), 719–760. https://doi.org/10.1029/RG026i004p00719

van der Meeren, C., Oksavik, K., Lorentzen, D., Moen, J. I., & Romano, V. (2014). GPS scintillation and irregularities at the front of an ionization tongue in the nightside polar ionosphere. *Journal of Geophysical Research: Space Physics*, *119*(10), 8624–8636. https://doi.org/10.1002/2014JA020114

Vickrey, J. F., & Kelley, M. C. (1982). The effects of a conducting E layer on classical F region cross-field plasma diffusion. *Journal of Geophysical Research*, *87*(A6), 4461–4468. https://doi.org/10.1029/JA087iA06p04461

Vickrey, J. F., Vondrak, R. R., & Matthews, S. J. (1981). The diurnal and latitudinal variation of auroral zone ionospheric conductivity. *Journal of Geophysical Research*, *86*(A1), 65–75. https://doi.org/10.1029/JA086iA01p00065

Wanliss, J. A., & Showalter, K. M. (2006). High-resolution global storm index: Dst versus SYM-H. *Journal of Geophysical Research*, *111*(A2), A02202. https://doi.org/10.1029/2005JA011034

Yamamoto, T., Ozaki, M., & Inoue, S. (2003). Relationship between ionospheric conductivity and intensity of the daytime region 1 field-aligned current in geomagnetically quiet conditions. *Journal of Geophysical Research*, *108*(A5), 1190. https://doi.org/10.1029/2002JA009607

Yeh, K. C., & Liu, C.-H. (1982). Radio wave scintillations in the ionosphere. *IEEE Proceedings*, *70*(4), 324–360. https://doi.org/10.1109/proc.1982.12313